Mechanisms for Iron Oxide Formation under Hydrothermal Conditions: An *in Situ* Total Scattering Study

Kirsten M. Ø. Jensen,[†,‡] Henrik L. Andersen,[†] Christoffer Tyrsted,[†] Espen D. Bøjesen,[†] Ann-Christin Dippel,[§] Nina Lock,[†] Simon J. L. Billinge,[‡,∥] Bo B. Iversen,[*,†] and Mogens Christensen[*,†]

[†]Center for Materials Crystallography, Department of Chemistry and iNANO, Aarhus University, DK-8000 Aarhus C, Denmark, [‡]Department of Applied Physics and Applied Mathematics, Columbia University, New York, New York 10027, United States, [§]Deutsches Elektronen-Synchrotron DESY, D-22607 Hamburg, Germany, and [∥]Condensed Matter Physics and Materials Science Department, Brookhaven National Laboratory, Upton, New York 11973, United States

ABSTRACT The formation and growth of maghemite (γ-Fe_2O_3) nanoparticles from ammonium iron(III) citrate solutions ($C_6O_7H_6 \cdot xFe^{3+} \cdot yNH_4$) in hydrothermal synthesis conditions have been studied by *in situ* total scattering. The local structure of the precursor in solution is similar to that of the crystalline coordination polymer $[Fe(H_2cit(H_2O)]_n$, where corner-sharing [FeO_6] octahedra are linked by citrate. As hydrothermal treatment of the solution is initiated, clusters of edge-sharing [FeO_6] units form (with extent of the structural order <5 Å). Tetrahedrally coordinated iron subsequently appears, and as the synthesis continues, the clusters slowly assemble into crystalline maghemite, giving rise to clear Bragg peaks after 90 s at 320 °C. The primary transformation from amorphous clusters to nanocrystallites takes place by condensation of the clusters along the corner-sharing tetrahedral iron units. The crystallization process is related to large changes in the local structure as the interatomic distances in the clusters change dramatically with cluster growth. The local atomic structure is size dependent, and particles smaller than 6 nm are highly disordered. The final crystallite size (<10 nm) is dependent on both synthesis temperature and precursor concentration.

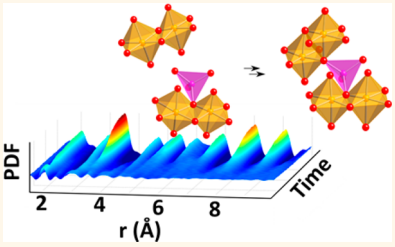

KEYWORDS: maghemite · hydrothermal · pair distribution function analysis · total scattering · *in situ*

Magnetic nanoparticles have recently received increasing attention due to potential applications such as improved permanent magnets,[1,2] magnetic storage media,[3] drug delivery, and medical imaging.[4−6] Of particular interest are magnetic iron oxides, *e.g.*, maghemite (γ-Fe_2O_3) and magnetite (Fe_3O_4). Both compounds are in the spinel structure family (Figure 1), where iron is found on sites with both octahedral (yellow) and tetrahedral (purple) coordination to oxygen. All iron in γ-Fe_2O_3 is in its ferric (Fe^{3+}) form in contrast to magnetite, which contains both Fe^{3+} and Fe^{2+}. Charge neutrality in γ-Fe_2O_3 is obtained by the formation of vacancies on the octahedral sites, and in bulk maghemite, the vacancy order gives rise to a superstructure where the unit cell is tripled along the *c* direction.[7]

γ-Fe_2O_3 is ferrimagnetic in its bulk form,[8] but for small nanocrystals, the particles exhibit superparamagnetic behavior. The magnetic performance is thus decisively dependent on crystallite size, and to obtain materials with tailor-made properties, it is crucial to control the nanoparticle characteristics during synthesis. To have industrial impact, the synthesis method must at the same time be scalable, environmentally friendly, energy efficient, simple, and cheap. In this context, the hydrothermal synthesis method is an excellent candidate, and significant research efforts have focused on applying the method to a broad range of functional materials[9,10] including magnetic iron oxide particles.[11−18] Numerous studies have established that by adjusting simple synthesis parameters such as precursor concentration, reaction temperature, or pressure, the characteristics of the product can be altered, thereby allowing property control.[19] The technique is now widely used in industry for nanoparticle production.[20−22]

While the hydrothermal method shows great promise, the fundamental chemical processes involved in particle formation and growth are still not fully understood. Obtaining further knowledge of the reaction

* Address correspondence to bo@chem.au.dk (B. B. Iversen) and mch@chem.au.dk (M. Christensen).

Received for review August 7, 2014 and accepted September 25, 2014.

Published online September 25, 2014
10.1021/nn5044096

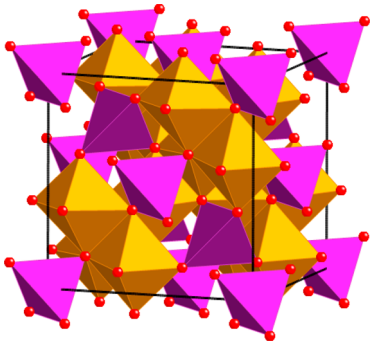

Figure 1. Maghemite structure in the space group $P4_32_12$. The yellow polyhedra show octahedrally coordinated iron, purple shows tetrahedrally coordinated iron, and the red spheres are oxide ions.

mechanisms is paramount for tailoring size, shape, and structure of novel nanocrystalline materials, and for this purpose, *in situ* studies of hydrothermal synthesis are extremely powerful.[23] By studying the chemical reactions *in situ* we get a glimpse into the very fundamental chemistry that takes place between inorganic species, which are only poorly understood compared to reactions in organic chemistry. During recent years, we and several other groups have done extensive *in situ* studies of the hydrothermal formation of various materials using especially powder X-ray diffraction (PXRD), providing important knowledge on the crystallite formation and growth.[23−35] However, to fully understand the formation of crystalline structures from a liquid or amorphous precursor, it is necessary to study the changes in atomic structure before and during the crystallization. For this purpose total scattering (TS) combined with pair distribution function (PDF) analysis is very well suited. As opposed to conventional crystallographic methods, TS allows extraction of structural information from amorphous, nanosized structures as well as fully crystalline particles, because information on both short- and long-range order can be obtained.[36,37] As we have recently demonstrated, the full crystallization process from ionic complexes through nanoclusters to crystalline materials can be followed.[38−41] In the present paper, we have studied the hydrothermal synthesis of maghemite from aqueous solutions of ammonium iron(III) citrate, which has been widely used in the synthesis of iron oxide nanoparticles and thin films for various applications.[15,42,43] While it has previously been suggested that this specific synthesis produces Fe_3O_4 nanocrystals, recent studies have shown that the product is predominantly γ-Fe_2O_3, as illustrated in the Supporting Information.[44] The total scattering investigations provide novel and surprising insight into how the tetrahedral and octahedral iron oxide units link to form the crystalline maghemite nanoparticles. The process involves large changes in the atomic arrangement during the crystallization, and PDF analysis reveals that Fe^{3+} in the precursor solution is embedded in a large citrate complex structure, which is decisive for the formation of γ-Fe_2O_3. The initially formed clusters are highly disordered and assemble slowly into crystals by condensation along the tetrahedral Fe site. The data additionally reveal new information on the size−structure relationship in maghemite, which is not accessible using conventional crystallographic methods.

RESULTS AND DISCUSSION

Iron Citrate Precursor Structure. Figure 2A shows the integrated *q*-space data from the ammonium iron(III) citrate precursor solution. The reddish-brown ammonium iron(III) citrate precursor is amorphous in its solid form and also when dissolved in water; only diffuse scattering is seen. In the corresponding PDF (Figure 2B), features to *ca.* 5 Å are observed, including a sharp, single peak at 2.0 Å agreeing with Fe−O bonds,[45] and further, less intense peaks at higher *r*-values. Features at lower *r*-values are also seen, corresponding to C−C and C−O bonds. Previous studies have suggested that Fe^{3+} and citrate molecules in solution form large iron-citrate complexes,[46−48] and our data show that the experimentally observed PDF from the ammonium iron citrate solution can be described based on the structure of crystalline $[Fe(H_2cit)(H_2O)]_n$, which has recently been reported.[49] The fit of this structure to the PDF is shown along with the data in Figure 2B, with further details given in the Supporting Information.

The structure of the iron complex used in the PDF refinement is shown in Figure 2C, where H has been left out for clarity. In bulk, the compound is a coordination polymer where partly deprotonated citric acid molecules link $[FeO_6]$ units through corner sharing of the octahedrons. Each iron site is coordinated to three citric acid molecules (Figure 2D). One is tridentate and coordinates to iron with two deprotonated carboxylate groups and the hydroxyl group, while two other citric acid molecules coordinate with only one deprotonated carboxyl group. An additional water molecule also coordinates to iron, resulting in a distorted $[FeO_6]$ octahedron, which is corner-sharing with the neighboring octahedron. The present data do not allow us to refine subtleties in the structure, and the actual citrate-iron coordination in the precursor solution may be slightly different from that illustrated. However, it is reasonable to suggest that the iron−iron coordination is closely related to a deprotonated form of $[Fe(H_2cit)(H_2O)]_n$, with a Fe−Fe distance of *ca.* 3.5 Å between the corner-sharing octahedra. The spatial extent of atomic correlations in the PDF indicate that the structure in the precursor solution is a dinuclear complex. Clear Fe−Fe correlations are not observed at *r*-values of >3.5 Å. However, it is likely that the precursor structure actually is polymeric in its nature, just like bulk $[Fe(H_2cit)(H_2O)]_n$,

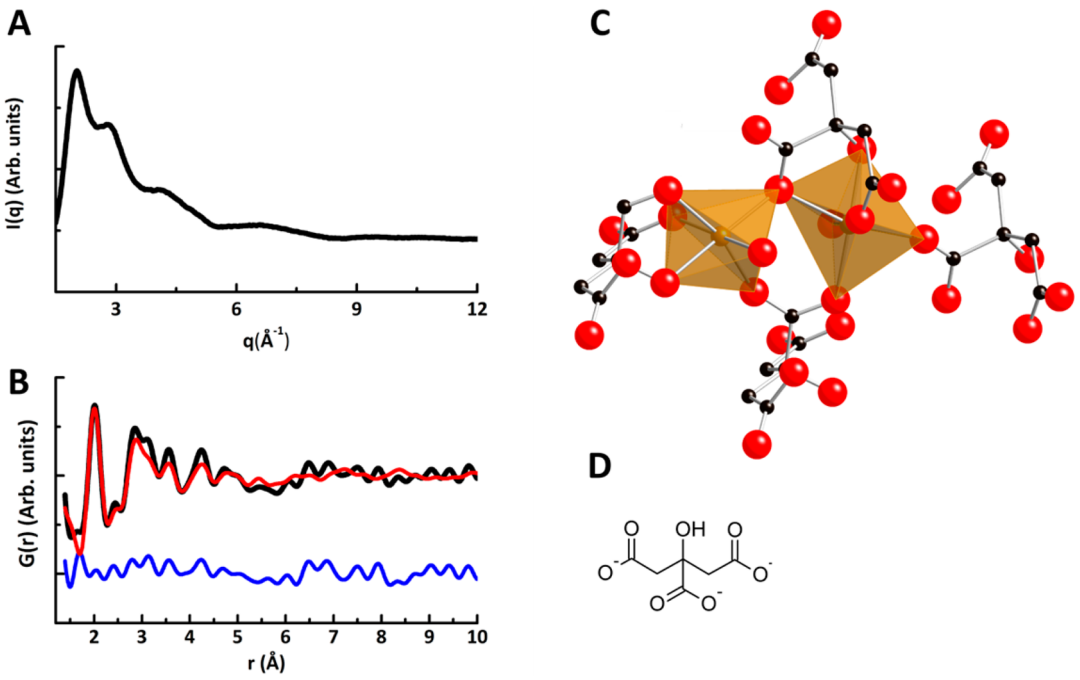

Figure 2. (A) Background-subtracted total scattering data from the aqueous precursor solution of ammonium iron citrate (q-range in the plot is limited to 12 Å^{-1}). (B) Black line: Corresponding PDF, showing structural features to *ca.* 5 Å. Red line: Fitted model of $[Fe(H_2cit)(H_2O)]_n$. Blue line: Difference curve between data and model. (C) Complex structure. The yellow polyhedra show octahedrally coordinated iron, the red spheres are oxygen, and the black spheres are carbon. Hydrogen atoms have been left out for clarity. (D) Citrate ligand group.

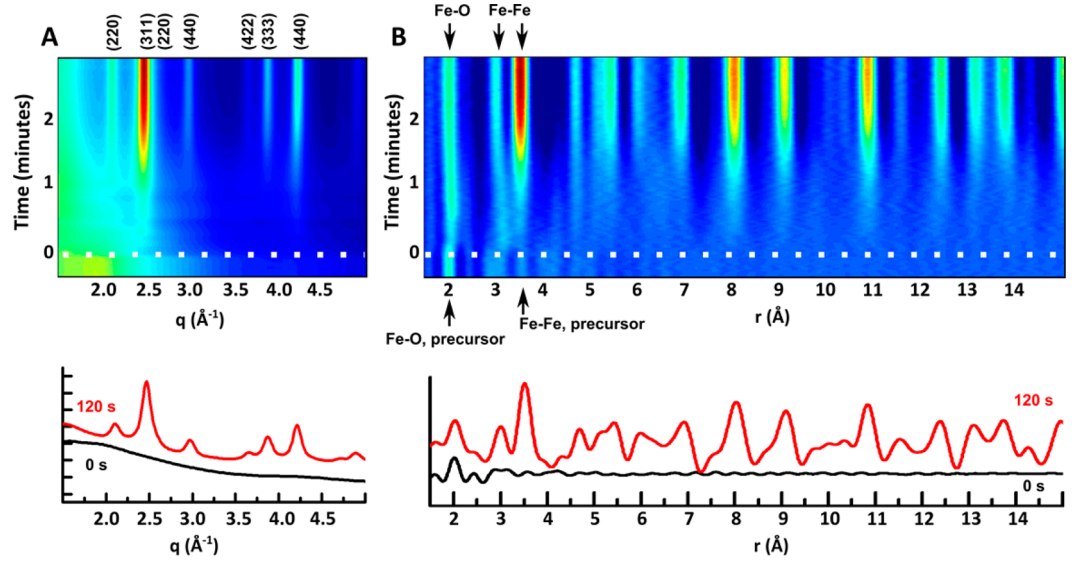

Figure 3. (A) Time-resolved q-space data obtained from the experiment done at 320 °C with 4 M ammonium iron(III) citrate solutions, plotted as a contour map. The *hkl* peaks arising from the $Fd\bar{3}m$ spinel structure are labeled. Selected data (from 0 and 120 s) are shown below. (B) Corresponding PDFs. Selected PDFs (from 0 and 120 s) are shown below. The intensity scale in the contour plots goes from blue through green and yellow to red.

but that this does not show up in the PDF due to a short polymer persistence length.[41]

The oxidation state of iron in the colorless $[Fe(H_2cit)(H_2O)]_n$ crystals is +II, while the ammonium iron citrate precursor contains only iron with oxidation state +III. The pH value of the reddish-brown 2 M precursor solution is ~6, and iron is thus assumed to be in the ferric state in the precursor complex.

Formation of Maghemite Nanoclusters. To follow the formation of γ-Fe_2O_3, the ammonium iron(III) citrate solutions were treated hydrothermally in our *in situ* capillary reactor at temperatures ranging from 270 to 370 °C and at 250 bar, as described in the experimental section.

As heating was initiated, the precursor citrate ions decomposed to CO, CO_2, and H_2O.[50,51] This decomposition was observed visually as small gas

bubbles appearing in the capillary, which subsequently redissolved in the liquid phase. The process is related to large changes in the scattering pattern as seen in the *q*-space data in Figure 3A, obtained during synthesis at 320 °C and 250 bar. From the corresponding PDFs (Figure 3B), these effects can be correlated to the atomic structure of the species in solution. As the synthesis is initiated at time = 0 s, the intensity of the precursor peaks between 2.5 and 5.5 Å decreases, revealing a change in Fe coordination. Simultaneously, a peak appears at 3.2 Å, and based on the rapidly increasing intensity, this is most likely a Fe−Fe correlation. A second peak soon after appears at ca. 3.5 Å, and at the same time, the Fe−O peak broadens, indicating the appearance of several different Fe−O bond distances. After *ca.* 90 s, intense Bragg and PDF peaks agreeing with the crystalline spinel structure are clearly seen, as described further below.

Note that we cannot distinguish the γ-Fe_2O_3 structure from Fe_3O_4 in the data, and we rely on *ex situ* Mössbauer and PXRD studies of the final product from the hydrothermal synthesis to determine that the primary product is maghemite and not magnetite, as discussed in the Supporting Information. Previous studies have suggested that CO, which forms during citrate decomposition, can partly reduce Fe^{3+} to Fe^{2+}, allowing formation of Fe_3O_4. However, our results indicate that this only happens to a very limited extent and that Fe is in the ferric form in both precursor and product.

TABLE 1. Atomic Pairs Contributing to the Low-*G*(*r*) PDF Peaks in the Bulk Maghemite Structure[7]

atoms in pair	interatomic distance	no. of pairs in unit cell
Fe_T−O	1.962 Å	32
Fe_O−O	2.017 Å	96
O−O	2.93 Å	48
Fe_O−Fe_O	2.99 Å	48
O−O	2.99 Å	96
O−O	3.05 Å	48
Fe_O−Fe_T	3.51 Å	96
Fe_T−O	3.51 Å	96
Fe_T−O	3.63 Å	32
Fe_T−Fe_T	3.66 Å	16

The atomic pairs contributing to the PDF peaks in the range 1.9−3.7 Å in the bulk spinel structure are listed in Table 1. The primary contribution to the peak at *ca.* 3.0 Å is the first correlation between octahedral iron sites (termed Fe_O−Fe_O), whereas that at 3.5 Å arises mainly due to the first correlations between the octahedral and tetrahedral sites (Fe_O−Fe_T). When considering the local order in the PDFs seen after *ca.* 10−20 s, the presence of the double peak between 2.9 and 3.5 Å indicates that two related Fe environments are seen in the nanoclusters. However, the evolution of the Fe−Fe correlations (Figure 4) shows that the Fe_O−Fe_T peak is not observed immediately after the citrate decomposition, suggesting that the primary clusters in the solution consist exclusively of edge-sharing [FeO_6] units with very short-range structural order (<5 Å). This interpretation is supported by the presence of the sharp Fe−O peak, showing one single Fe environment. We would expect this to broaden if there were tetrahedral iron in the cluster because of the slightly shorter Fe−O distance in the tetrahedral coordination. The evolution of the PDFs thus points toward a mechanism where the initial nanoclusters consist of edge-sharing [FeO_6] octahedra, which are built from the corner-sharing octahedrons in the

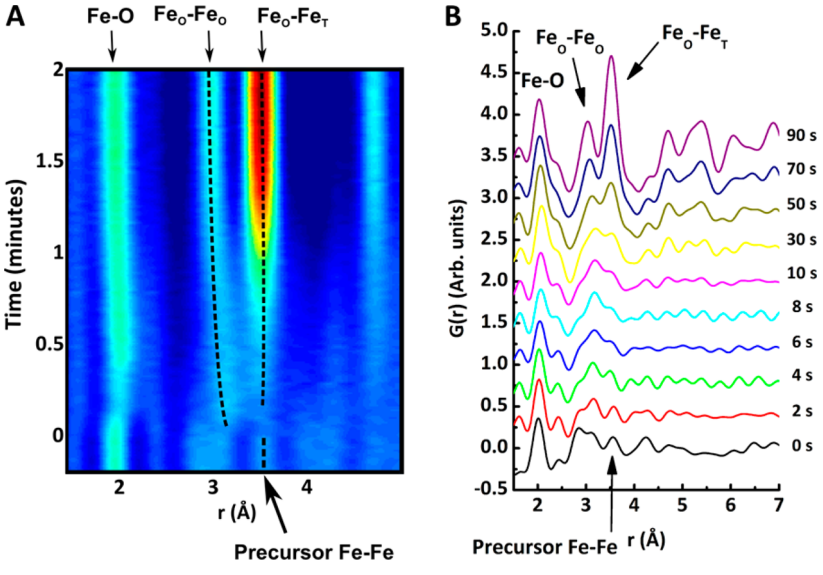

Figure 4. (A) Contour plot of the low *r*-range PDFs obtained at 320 °C and 4 M ammonium iron citrate. The dotted lines are guides to the eyes showing the evolution of the Fe−Fe peaks. (B) Selected PDFs from the initial stages in the synthesis at 320 °C, 4 M.

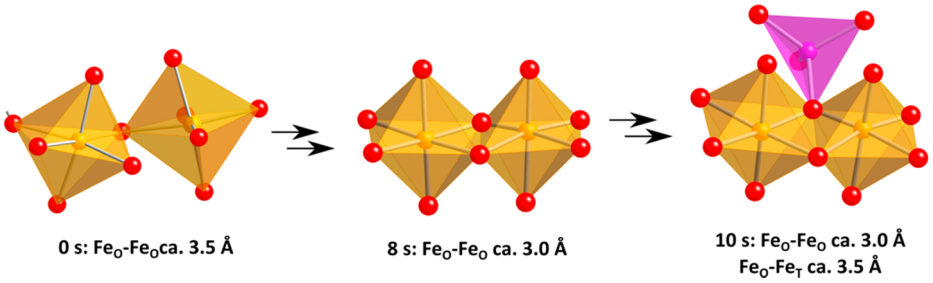

Figure 5. Structures observed in the low *r*-region of the initially observed PDFs. The yellow polyhedra show octahedrally coordinated iron, the purple polyhedron shows tetrahedrally coordinated iron, and the red spheres show oxygen.

precursor complex when the organic ligand molecules decompose. However, after ~10 s, a peak at 3.5 Å appears and the cluster structure can now be described as a nanoscale, disordered maghemite-like assembly of both tetrahedrally (corner-sharing) and octahedrally (edge-sharing) coordinated iron atoms. The process is illustrated in Figure 5.

Considering the stability of the iron ions in conventional crystal field stabilization energy (CFSE), octahedral coordination is preferred for Fe^{2+}, while octahedral and tetrahedral coordination are equally favorable for Fe^{3+}.[52] However, in acidic and neutral aqueous solutions, octahedrally coordinated iron is more commonly observed,[53,54] and when dissolving a simple salt such as $FeCl_3$ in water, the octahedral $[FeCl_x(H_2O)_{6-x}]$ complex forms.[55−58] In a recent study, we observed how solutions of $Fe(NO_3)_3 \cdot 9H_2O$ produce hematite, α-Fe_2O_3, where all iron atoms are octahedrally coordinated when hydrothermally treated.[35] Other reports have also stated how, for example, iron chloride solutions and iron oxalate[58] generates hematite in hydrothermal synthesis conditions. The appearance of the tetrahedrally coordinated iron is thus surprising and indicates the importance of the citrate group in the synthesis of maghemite. The citrate coordination and decomposition process must play a significant role in the formation of the nanoclusters. Possibly, the degradation of the tridentate citrate ligand groups lowers the coordination of some of the iron ions, giving rise to the tetrahedrally coordinated iron, although coordination to water in the solution could work against this effect. On the basis of the present data we can only propose a model, and further studies of the citrate degradation are needed to understand the coordination change in detail.

From Clusters to Nanocrystals: Changes in Local Structure. As the reaction proceeds, the intensity of the Fe_O-Fe_T peak (at *ca.* 3.5 Å) increases and the ratio between the Fe_O-Fe_O and Fe_O-Fe_T peak shifts (see Figure 4). The evolution of the local structure thus shows a rapidly increasing number of correlations between octahedral and tetrahedral iron as the particles form. This behavior is seen in data from all performed experiments, as shown in Figures S1−S8 in the Supporting Information. Simultaneously with the Fe_O-Fe_T intensity increase,

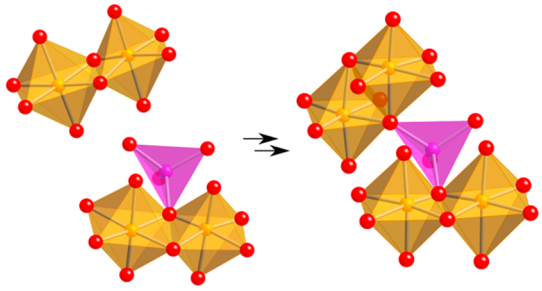

Figure 6. Cluster growth by condensation along tetrahedrally coordinated iron atoms.

PDF features at higher *r*-values are observed (Figure 3B shows peaks up to 15 Å after 60 s), and in *q*-space (Figure 3A), very weak and broad diffraction peaks become visible.

Numerous processes including a variety of iron oxide cluster structures (with structural order up to *ca.* 15 Å) could give rise to the changes observed in the data. However, a generalized mechanism that accounts for the simultaneous evolution of local and long-range order is depicted in Figure 6. After the formation of small clusters containing octahedral and tetrahedral units as explained above, the clusters assemble and produce larger structures. On the basis of the intensity increase of the Fe_O-Fe_T peak, the condensation of the smaller cluster appears to take place mainly along the tetrahedral Fe units, as illustrated in Figure 6. In the process depicted, the Fe_O-Fe_T peak of the product has double the intensity compared to that of the reactants, whereas the Fe_O-Fe_O peak is left unchanged, in agreement with the observed data. The initially formed clusters thus assemble by the corner-sharing, tetrahedrally coordinated iron ions to form disordered particles with some long-range order, but with extensive defects in the structure. The condensation along the tetrahedral irons is possibly favorable over the octahedral iron because only one new bond must be created. The geometry of the tetrahedral site may also allow enough space for cluster assembly.

It is important to note that the cluster growth illustrated in Figure 6 is one possible representation of the process describing the features and changes observed in the early stages of the synthesis. Several

alternative combinations of octahedrally and tetrahedrally coordinated iron ions may be present simultaneously, and the fast evolution of long-range order indicates that the clusters promptly condensate into significantly larger structures than depicted in Figure 6. However, the primary assembly along the corner-sharing Fe_T units into disordered structures appears to be the general mechanism responsible for cluster growth in the present synthesis. From combined SAXS/PXRD investigations[15] it is known that the crystallites grow from free clusters in solution, rather than from a larger structural amorphous network. This agrees with the total scattering observations and shows that the particles grow by cluster assembly rather than as a solid-state transformation from an amorphous network phase, as has been shown to be the case in yttria-stabilized zirconia nanoparticles, for example.[41]

To extract structural information from the cluster growth, the PDFs were modeled using the maghemite $P4_32_12$ structure. This is a subgroup of the general $Fd\bar{3}m$ spinel structure and is often used to describe γ-Fe_2O_3 when refinements in the large $P4_12_12$ unit cell with vacancy ordering are not feasible or appropriate (see discussion in the Supporting Information).[7,59] In the refinements, the *r*-range below 2.6 Å (*i.e.*, the first Fe−O distances) was not included, as this peak was seen to be much more intense in the data than in the calculated model (see Supporting Information, S9), which is due to the presence of terminal Fe−O/H_2O bonds and/or unbound [FeO_6] units covering the extensive surface of the small clusters. Examples of fits to the data are shown in Figure 7, with further details given in the Supporting Information.

Figure 8A shows the occupancy of the tetrahedral *8a* site as a function of time for different temperatures and precursor concentrations. In the bulk maghemite structure, this value is 1. Clearly, a large deficiency of Fe_T is seen in the refined crystal structure of the initially formed particles, but with synthesis time and temperature, a defect-free maghemite structure is obtained. Precursor concentration has little effect on the defect concentration. The defects are related to the low intensity of the Fe_O−Fe_T peak described above and again illustrate how the initially formed particles primarily consist of octahedral units.

Figure 8B shows the tetrahedral site occupancy plotted as a function of particle size (expressed through the refined spherical particle diameter) for four different experiments. All four curves are overlapping, implying that independently of the synthesis conditions, there is a direct correlation between particle size and Fe_T site occupancy. This suggests that the Fe_T defect may be related to surface effects. Possibly, many of the defective Fe_T sites in the structure are situated at or near the large particle surface and are

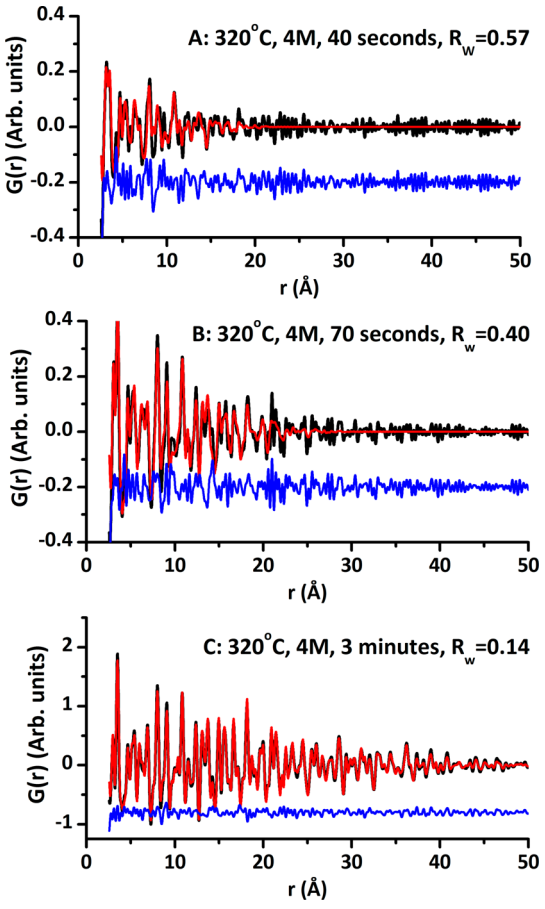

Figure 7. Examples of PDF fits in the range *r* = 2.650 Å. The black line shows the experimental PDF, the red line the modeled PDF, and the blue line the difference between the two. The difference curve has been offset for clarity. Note the difference in scale between A, B, and C, expanding the difference curve.

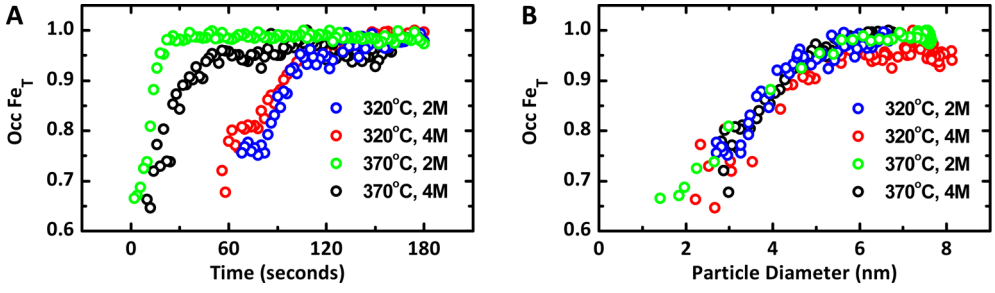

Figure 8. Occupancy of Fe_T as a function of time (A) and particle size (B). Data from four different experiments are shown.

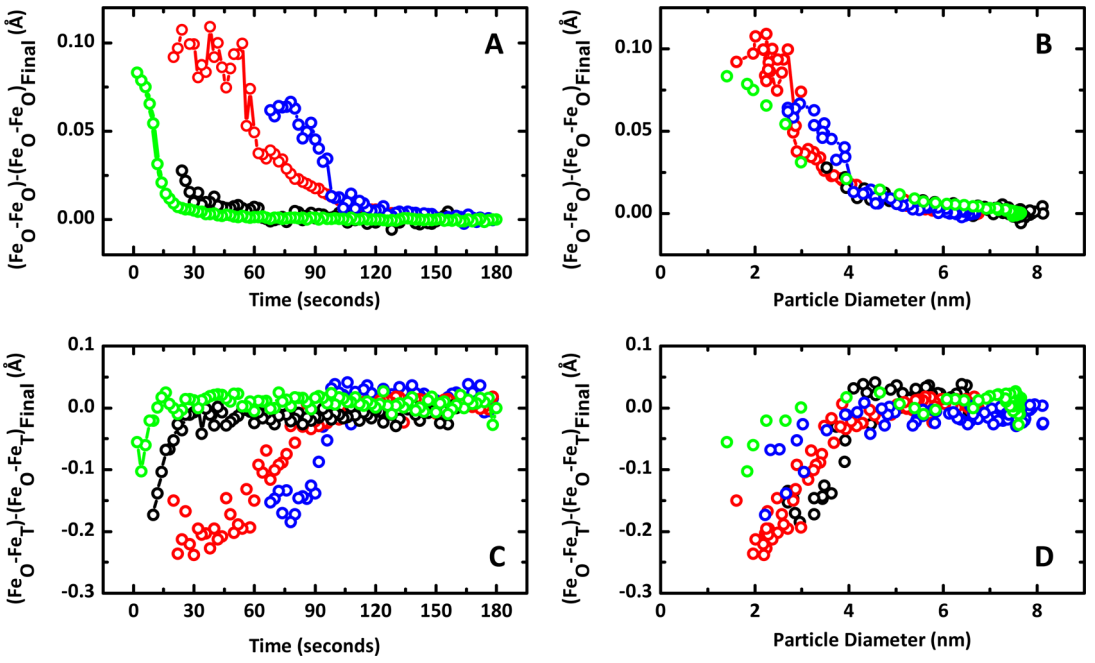

Figure 9. Change of Fe_O—Fe_O distance plotted as a function of (A) time and (B) size (spherical-particle diameter). Change of Fe_O—Fe_O distance plotted as a function of (C) time and (D) sp-diameter. Blue: 2 M, 320 °C. Red: 4 M, 320 °C. Green: 2 M, 370 °C. Black: 4 M, 370 °C.

thus not part of the 3D crystalline lattice. Only as the particles grow by further cluster assembly are the sites occupied and fully connected to the core structure. The possible relation between Fe_T defects and surface structure supports the hypothesis that the tetrahedrally coordinated iron plays an important role in the cluster condensation mechanism leading to particle growth as illustrated in Figure 6.

Changes in interatomic distances are seen simultaneously with increased occupation of the crystallographic Fe_T site. The change in distance is shown in the time-dependent evolution of the Fe_O—Fe_O distance, plotted in Figure 9A. The distance is initially elongated compared to the bulk structure, but as the particles crystallize, the interatomic distance approaches a final equilibrium value. In Figure 9B, the Fe_O—Fe_O distance is plotted as a function of the particle size. The correlation between size and bond length is again independent of the synthesis conditions as the curves from 320 and 370 °C and 2 and 4 M overlap. This could again suggest that the elongated interatomic distances are related to the surface structure. In the surface layer, the [FeO_6] octahedra are not constrained in a crystalline lattice but possibly have some freedom to move, which may explain the elongated Fe_O—Fe_O distances. It may also be that sufficient lattice energy is required to prevent the structural relaxation that leads to elongated Fe_O—Fe_O bonds in the particles. Only as the extent of the crystalline lattice grows does the energy gained by approaching the ordered spinel structure lead to the bulk Fe_O—Fe_O bond length.

The structural changes are closely reflected in the unit cell parameter, plotted against crystallite size in

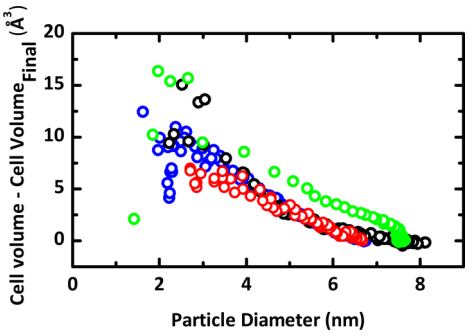

Figure 10. Change in unit cell volume as a function of particle diameter. Blue: 2 M, 320 °C. Red: 4 M, 320 °C. Green: 2 M, 370 °C. Black: 4 M, 370 °C.

Figure 10. This has previously been observed, and due to the PDF analysis of the local structure, we can now assign this to the elongated Fe_O—Fe_O distance.[15]

The Fe_O—Fe_T distance is plotted as a function of synthesis time in Figure 9C. Although the uncertainties on the refined values (seen from the highly scattered data points) are large due to the low occupancy of Fe_T, the refinements surprisingly show that the initial distance between the Fe_O and Fe_T is shorter than in bulk maghemite. Possibly, as the initially formed clusters consisting mainly of octahedral iron are linked together by Fe_T (Figure 6) to form crystalline γ-Fe_2O_3, the distance between Fe_T and Fe_O stretches to accommodate the various structural units in the maghemite crystal lattice. However, the overall effect is smaller than the change in Fe_O—Fe_O distance, as this behavior dictates the change in unit cell parameter. The Fe_O—Fe_T distance is plotted as a

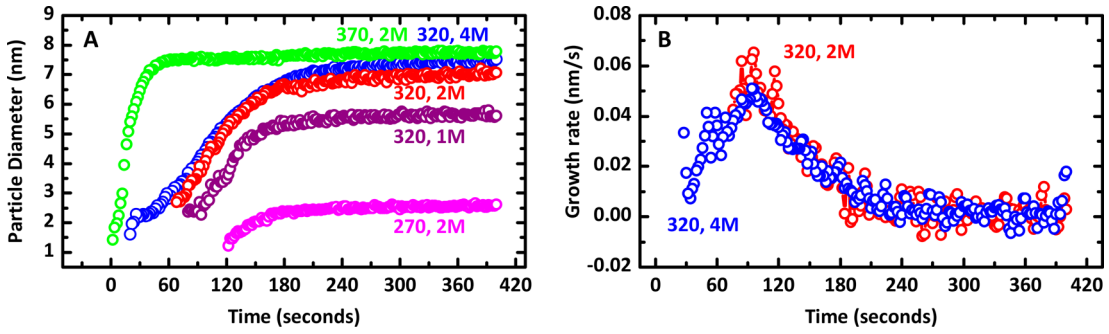

Figure 11. (A) Refined sp-diameter, plotted as a function of time for different temperatures and precursor concentrations. (B) Differentiated growth curves (growth rates) for experiments done at 320 °C, using 2 and 4 M precursor. Before differentiation, the growth curves were smoothed over an interval of 5 points.

function of crystallite size in Figure 9D, and again, a clear structure−size relation is seen.

The results point toward a mechanism where locally ordered clusters quickly assemble into loosely bound particles with some intermediate range order, but with a large number of defects. Slowly, the structure orders and starts crystallizing as the particles grow by cluster condensation at the surface. Particles smaller than 6 nm are highly defective due to the formation mechanism in the hydrothermal synthesis. At 320 °C, it takes almost 2 min until ordered maghemite is obtained, and while the same formation mechanism is seen at 370 °C, the bulk maghemite structure appears much faster. Precursor concentration has almost no influence on the reaction rate. The disorder will most probably affect the magnetic properties of the nanoparticles, and the formation mechanisms must therefore be considered when designing maghemite synthesis processes.[60,61]

Interestingly, bulk maghemite shows vacancy ordering on the octahedral sites, while the tetrahedral iron site is always fully occupied. The *in situ* data do not allow us to follow the distribution of vacancies on Fe_O as a function of time or particle size, but previous studies have shown that in the early stages of the synthesis the vacancies are disordered.[7] This seems very likely from the complex formation mechanism.

Particle Growth and Growth Rate. The growth curves obtained from the sequential PDF refinements are seen in Figure 11A. The final particle size is dependent on temperature and precursor concentration, and the largest crystallites are seen when increasing both parameters. This is in agreement with previous results from Scherrer analysis of *in situ* PXRD data of iron oxide growth[15] as well as recent studies of the evolution of particle size distribution during maghemite synthesis.[35] The same range of particle sizes is seen from TEM images of the final product from the hydrothermal synthesis, shown in the Supporting Information.

The time-dependent growth rates (differentiated growth curves) of the experiments done at 320 °C using 2 and 4 M precursor solutions are plotted in Figure 11B. The growth rate initially increases and reaches a maximum after *ca.* 90 s before decreasing. This maximum can be directly related to the cluster condensation mechanisms, as the peak in growth rate is seen at the exact same time as the bulk bond lengths and full Fe_T occupancy is obtained. The same trend is observed for other synthesis conditions, as seen in the Supporting Information. The primary growth of the particles thus happens in the initial condensation phase, before particles with the ordered crystal structure are obtained. After the disordered clusters have assembled and condensed to particles of *ca.* 4−5 nm, only limited growth to ca. 7 nm is seen. Possibly, the energy required for particle growth is lower before crystallization, where the large amount of defects in the disordered structure may mediate particle growth. As the particles have crystallized, more dramatic structural changes are needed for further growth. Often, nanoparticle growth is considered in terms of, for example, Ostwald ripening or oriented attachment after the formation of crystallites. Our study indicates that this growth stage is less significant than the primary cluster assembly and illustrates the importance of characterizing the structures appearing before long-range order occurs.

CONCLUSIONS

By means of total scattering and PDF analysis, the formation and growth of maghemite nanoparticles from aqueous ammonium iron(III) citrate solutions have been followed. The local atomic structure of the precursor solution is closely related to that of crystalline $[Fe(H_2cit)(H_2O)]_n$, having corner-sharing octahedrally coordinated Fe^{3+} in a polymer-like structure linked by citrate molecules. Nanoclusters consisting of edge-sharing $[FeO_6]$ units form immediately during the hydrothermal treatment, and tetrahedrally coordinated iron ions are observed after a short time (less than 10 s at 320 °C). The clusters subsequently assemble to give rise to highly disordered maghemite particles, which order during further particle growth. The cluster assembly takes place mainly along the tetrahedral sites that link the octahedrally coordinated iron oxide units.

The study illustrates how characterizing the precrystalline steps is crucial for understanding inorganic hydrothermal synthesis. Often, particle formation and growth in hydrothermal synthesis are considered as single atoms or molecules coming together to form an isotropic particle, much as is the case in crystallization in a melt. However, our results show that hydrothermal synthesis represents a much more complex case, where the continual units are clusters and where dramatic changes in the local structure must be taken into account when considering reaction kinetics. Both chemical and geometric factors play important roles in the formation processes. Combined with PDF analysis, total scattering methods allow for characterization of the structures present in the precrystalline steps, allowing in-depth insight into the important processes related to nanoparticle crystallization.

METHODS

***In Situ* Experiments.** *In situ* total scattering experiments were done at beamline ID11[62] at the ESRF, Grenoble, France, and at beamline P02.1 at PETRAIII, Hamburg, Germany. The experimental setup has been described in detail elsewhere.[63] The reactor consists of a thin fused silica tube measuring 0.6 mm in inner diameter and 0.05 mm in wall thickness, ensuring a high transmission of X-rays. The tube was mounted in the setup using Swagelok fittings, pressurized with deionized water and heated using a jet of hot air, while simultaneously collecting X-ray diffraction patterns during sequential exposures. The efficiency of the heater combined with the small volume of the capillary ensures very fast heating, and the desired temperature was reached within seconds after initiation of the experiment.[59]

The precursor for the iron oxide particles was aqueous solutions of ammonium iron(III) citrate ($C_6H_8O_7 \cdot x$Fe(III)$\cdot y NH_3$) (Sigma-Aldrich, reagent grade, assuming M = 265.0 g/mol) at various concentrations (1−4 M). The solid reactant easily dissolved in deionized water at room temperature, producing clear, reddish-brown solutions. The pH value of the 2 M solution was measured to be 6.0. For all experiments, the pressure was set to 250 bar, whereas the temperature was varied between 270 and 370 °C.

The heatgun exhaust creates a temperature gradient over the capillary reactor, with a broad temperature maximum at the center of the reactor. The X-ray beam always hits the center position of the capillary, and the reported temperatures and data represent the reaction at this point.

For the experiments performed at the ESRF, the wavelength was 0.1897 Å and a Frelon 4 M CCD detector was used with a sample−detector distance of 10 cm, resulting in a q_{max} value of 23.5 Å^{-1}. The time resolution for the ESRF data was 2 s. At PETRA III, the detector was a PerkinElmer XRD1621 amorphous silicon detector. With an X-ray wavelength of 0.2072 Å and a detector distance of 23 cm, the q_{max} available was 21 Å^{-1}. The time resolution for the data collection at PETRA III was 3 s.

Data Analysis. For all experiments, the raw 2D scattering images were integrated in Fit2D,[64] and PDFs were subsequently obtained using PDFgetX3.[65] The scattering pattern obtained from the capillary containing deionized water at the appropriate conditions was subtracted from the integrated pattern before Fourier transformation. The q-range used in the Fourier transform was limited to 1−17 Å^{-1} due to low statistics at higher scattering angles. The resulting PDFs were modeled to extract structural parameters using PDFgui.[66] The precursor structure was refined based on the structure of $[Fe(H_2cit)(H_2O)]_n$ (cit = citrate).[49] The γ-Fe_2O_3 structure was described in space group $P4_32_12$[55] and refined in the r-range from 2.6 to 50 Å. Here, the scale factor, crystallite size (spherical particle diameter), unit cell, iron coordinates, and occupancy on the tetrahedral site were refined. The refinements of the time-resolved PDFs were done sequentially starting from the last frame with the crystalline phase. The thermal parameters were refined in the last frame and kept fixed at the resulting values in the sequential refinements.

Conflict of Interest: The authors declare no competing financial interest.

Acknowledgment. This work was supported by the Danish National Research Foundation (Center for Materials Crystallography, DNRF93), the Danish Research Council for Technology and Production Sciences (Improved Permanent Magnets through Nanosctructuring), and the Danish Research Council for Nature and Universe (Danscatt). K.M.ØJ is funded by the Individual Postdoc Grant program from the Villum Foundation. S.J.L.B. acknowledges funding from U.S. DOE under contract no. DE-AC02-98CH10886. We are grateful for beamtime granted at PO2.1 at PETRA III and at ID11 at the European Synchrotron Radiation Facility and thank G. Vaughan for assistance in using beamline ID11. Haraldur P. Gunnlaugsson is thanked for Mössbauer data collection and analysis.

Supporting Information Available: Mössbauer data showing maghemite as the main product; contour plots of PDFs obtained from all additional experiments; details on PDF refinements of the precursor structure, results from refinements of maghemite structure; TEM images; particle growth rates. This material is available free of charge *via* the Internet at http://pubs.acs.org.

REFERENCES AND NOTES

1. Zeng, H.; Li, J.; Liu, J. P.; Wang, Z. L.; Sun, S. H. Exchange-Coupled Nanocomposite Magnets by Nanoparticle Self-Assembly. *Nature* **2002**, *420*, 395–398.
2. Jones, N. The Pull of Stronger Magnets. *Nature* **2011**, *472*, 22–23.
3. Lu, A. H.; Salabas, E. L.; Schuth, F. Magnetic Nanoparticles: Synthesis, Protection, Functionalization, and Application. *Angew. Chem., Int. Ed.* **2007**, *46*, 1222–1244.
4. Pankhurst, Q. A.; Connolly, J.; Jones, S. K.; Dobson, J. Applications of Magnetic Nanoparticles in Biomedicine. *J. Phys. D: Appl. Phys.* **2003**, *36*, R167–R181.
5. Pankhurst, Q. A.; Thanh, N. T. K.; Jones, S. K.; Dobson, J. Progress in Applications of Magnetic Nanoparticles in Biomedicine. *J. Phys. D: Appl. Phys.* **2009**, *42*, 224001.
6. Berry, C. C. Progress in Functionalization of Magnetic Nanoparticles for Applications in Biomedicine. *J. Phys. D: Appl. Phys.* **2009**, *42*, 224003.
7. Jorgensen, J. E.; Mosegaard, L.; Thomsen, L. E.; Jensen, T. R.; Hanson, J. C. Formation of γ-Fe_2O_3 Nanoparticles and Vacancy Ordering: An *in Situ* X-ray Powder Diffraction Study. *J. Solid State Chem.* **2007**, *180*, 180–185.
8. Dronskowski, R. The Little Maghemite Story: A Classic Functional Material. *Adv. Funct. Mater.* **2001**, *11*, 27–29.
9. Byrappa, K.; Adschiri, T. Hydrothermal Technology for Nanotechnology. *Prog. Cryst. Growth Charact. Mater.* **2007**, *53*, 117–166.
10. Aymonier, C.; Loppinet-Serani, A.; Reveron, H.; Garrabos, Y.; Cansell, F. Review of Supercritical Fluids in Inorganic Materials Science. *J. Supercrit. Fluids* **2006**, *38*, 242–251.
11. Ni, S. B.; Lin, S. M.; Pan, Q. T.; Yang, F.; Huang, K.; He, D. Y. Hydrothermal Synthesis and Microwave Absorption Properties of Fe_3O_4 Nanocrystals. *J. Phys. D: Appl. Phys.* **2009**, *42*, 055004.
12. Daou, T. J.; Pourroy, G.; Begin-Colin, S.; Greneche, J. M.; Ulhaq-Bouillet, C.; Legare, P.; Bernhardt, P.; Leuvrey, C.;

Rogez, G. Hydrothermal Synthesis of Monodisperse Magnetite Nanoparticles. *Chem. Mater.* **2006**, *18*, 4399–4404.
13. Zhang, Z. J.; Chen, X. Y.; Wang, B. N.; Shi, C. W. Hydrothermal Synthesis and Self-Assembly of Magnetite (Fe_3O_4) Nanoparticles with the Magnetic and Electrochemical Properties. *J. Cryst. Growth* **2008**, *310*, 5453–5457.
14. Khollam, Y. B.; Dhage, S. R.; Potdar, H. S.; Deshpande, S. B.; Bakare, P. P.; Kulkarni, S. D.; Date, S. K. Microwave Hydrothermal Preparation of Submicron-Sized Spherical Magnetite (Fe_3O_4) Powders. *Mater. Lett.* **2002**, *56*, 571–577.
15. Bremholm, M.; Felicissimo, M.; Iversen, B. B. Time-Resolved *in Situ* Synchrotron X-ray Study and Large-Scale Production of Magnetite Nanoparticles in Supercritical Water. *Angew. Chem., Int. Ed.* **2009**, *48*, 4788–4791.
16. Horner, O.; Neveu, S.; de Montredon, S.; Siaugue, J. M.; Cabuil, V. Hydrothermal Synthesis of Large Maghemite Nanoparticles: Influence of the pH on the Particle Size. *J. Nanopart. Res.* **2009**, *11*, 1247–1250.
17. Adschiri, T.; Kanazawa, K.; Arai, K. Rapid and Continuous Hydrothermal Crystallization of Metal Oxide Particles in Supercritical Water. *J. Am. Ceram. Soc.* **1992**, *75*, 1019–1022.
18. Cabanas, A.; Poliakoff, M. The Continuous Hydrothermal Synthesis of Nano-Particulate Ferrites in Near Critical and Supercritical Water. *J. Mater. Chem.* **2001**, *11*, 1408–1416.
19. Walton, R. I. Subcritical Solvothermal Synthesis of Condensed Inorganic Materials. *Chem. Soc. Rev.* **2002**, *31*, 230–238.
20. Lester, E.; Blood, P.; Denyer, J.; Giddings, D.; Azzopardi, B.; Poliakoff, M. Reaction Engineering: The Supercritical Water Hydrothermal Synthesis of Nano-Particles. *J. Supercrit. Fluids* **2006**, *37*, 209–214.
21. Adschiri, T.; Lee, Y. W.; Goto, M.; Takami, S. Green Materials Synthesis with Supercritical Water. *Green Chem.* **2011**, *13*, 1380–1390.
22. Yoshimura, M.; Byrappa, K. Hydrothermal Processing of Materials: Past, Present and Future. *J. Mater. Sci.* **2008**, *43*, 2085–2103.
23. Jensen, K. M. Ø.; Tyrsted, C.; Bremholm, M.; Iversen, B. B. *In-Situ* Studies of Solvothermal Synthesis of Energy Materials. *ChemSusChem* **2014**, *7*, 1594–1611.
24. Bremholm, M.; Jensen, H.; Iversen, S. B.; Iversen, B. B. Reactor Design for *in Situ* X-ray Scattering Studies of Nanoparticle Formation in Supercritical Water Syntheses. *J. Supercrit. Fluids* **2008**, *44*, 385–390.
25. Tyrsted, C.; Becker, J.; Hald, P.; Bremholm, M.; Pedersen, J. S.; Chevallier, J.; Cerenius, Y.; Iversen, S. B.; Iversen, B. B. *In-Situ* Synchrotron Radiation Study of Formation and Growth of Crystalline $Ce_xZr_{1-x}O_2$ Nanoparticles Synthesized in Supercritical Water. *Chem. Mater.* **2010**, *22*, 1814–1820.
26. Mi, J. L.; Christensen, M.; Tyrsted, C.; Jensen, K. M. Ø.; Becker, J.; Hald, P.; Iversen, B. B. Formation and Growth of Bi_2Te_3 in Biomolecule-Assisted Near-Critical Water: *In Situ* Synchrotron Radiation Study. *J. Phys. Chem. C* **2010**, *114*, 12133–12138.
27. Jensen, K. M. Ø.; Christensen, M.; Tyrsted, C.; Bremholm, M.; Iversen, B. B. Structure, Size, and Morphology Control of Nanocrystalline Lithium Cobalt Oxide. *Cryst. Growth Des.* **2011**, *11*, 753–758.
28. Jensen, K. M. Ø.; Christensen, M.; Tyrsted, C.; Iversen, B. B. Real-Time Synchrotron Powder X-ray Diffraction Study of the Antisite Defect Formation during Sub- and Supercritical Synthesis of $LiFePO_4$ and $LiFe_{1-x}Mn_xPO_4$ Nanoparticles. *J. Appl. Crystallogr.* **2011**, *44*, 287–294.
29. Laumann, A.; Jensen, K. M. Ø.; Tyrsted, C.; Bremholm, M.; Fehr, K. T.; Holzapfel, M.; Iversen, B. B. In-Situ Synchrotron X-ray Diffraction Study of the Formation of Cubic Li_2TiO_3 Under Hydrothermal Conditions. *Eur. J. Inorg. Chem.* **2011**, *2011*, 2221–2226.
30. Tyrsted, C.; Pauw, B. R.; Jensen, K. M. O.; Becker, J.; Christensen, M.; Iversen, B. B. Watching Nanoparticles Form: An *In Situ* (Small-/Wide-Angle X-ray Scattering/Total Scattering) Study of the Growth of Yttria-Stabilised Zirconia in Supercritical Fluids. *Chem.—Eur. J.* **2012**, *18*, 5759–5766.
31. Zhou, Y.; Antonova, E.; Lin, Y. H.; Grunwaldt, J. D.; Bensch, W.; Patzke, G. R. *In Situ* X-ray Absorption Spectroscopy/Energy-Dispersive X-ray Diffraction Studies on the Hydrothermal Formation of $Bi_2W_{1-x}Mo_xO_6$ Nanomaterials. *Eur. J. Inorg. Chem.* **2012**, 783–789.
32. Walton, R. I.; O'Hare, D. Watching Solids Crystallise Using *in Situ* Powder Diffraction. *Chem. Commun.* **2000**, *2*, 2283–2291.
33. Ok, K. M.; Lee, D. W.; Smith, R. I.; O'Hare, D. Time-Resolved *in Situ* Neutron Diffraction under Supercritical Hydrothermal Conditions: A Study of the Synthesis of $KTiOPO_4$. *J. Am. Chem. Soc.* **2012**, *134*, 17889–17891.
34. Cheetham, A. K.; Mellot, C. F. *In Situ* Studies of the Sol-Gel Synthesis of Materials. *Chem. Mater.* **1997**, *9*, 2269–2279.
35. Andersen, H. L.; Jensen, K. M. O.; Tyrsted, C.; Bojesen, E. D.; Christensen, M. Size and Size Distribution Control of γ-Fe_2O_3 Nanocrystallites: An *in Situ* Study. *Cryst. Growth Des.* **2014**, *14*, 1307–1313.
36. Billinge, S. J. L.; Kanatzidis, M. G. Beyond Crystallography: The Study of Disorder, Nanocrystallinity and Crystallographically Challenged Materials with Pair Distribution Functions. *Chem. Commun.* **2004**, 749–760.
37. Billinge, S. J. L. Nanostructure Studied Using the Atomic Pair Distribution Function. *Z. Kristallogr.* **2007**, 17–26.
38. Jensen, K. M. O.; Christensen, M.; Juhas, P.; Tyrsted, C.; Bojesen, E. D.; Lock, N.; Billinge, S. J. L.; Iversen, B. B. Revealing the Mechanisms behind SnO_2 Nanoparticle Formation and Growth during Hydrothermal Synthesis: An *In Situ* Total Scattering Study. *J. Am. Chem. Soc.* **2012**, *134*, 6785–6792.
39. Tyrsted, C.; Jensen, K. M. O.; Bojesen, E. D.; Lock, N.; Christensen, M.; Billinge, S. J. L.; Iversen, B. B. Understanding the Formation and Evolution of Ceria Nanoparticles under Hydrothermal Conditions. *Angew. Chem., Int. Ed.* **2012**, *51*, 9030–9033.
40. Saha, D.; Jensen, K. M. Ø.; Tyrsted, C.; Bøjesen, E. D.; Mamakhel, A. H.; Dippel, A.-C.; Christensen, M.; Iversen, B. B. *In Situ* Total X-Ray Scattering Study of WO_3 Nanoparticle Formation under Hydrothermal Conditions. *Angew. Chem., Int. Ed.* **2014**, *53*, 3667–3670.
41. Tyrsted, C.; Lock, N.; Jensen, K. M. O.; Christensen, M.; Bojesen, E. D.; Emerich, H.; Vaughan, G.; Billinge, S. J. L.; Iversen, B. B. Evolution of Atomic Structure during Nanoparticle Formation. *IUCrJ.* **2014**, *1*, 165–171.
42. Adschiri, T.; Hakuta, Y.; Arai, K. Hydrothermal Synthesis of Metal Oxide Fine Particles at Supercritical Conditions. *Ind. Eng. Chem. Res.* **2000**, *39*, 4901–4907.
43. Park, S. Preparation of Iron Oxides using Ammonium Iron Citrate Precursor: Thin Films and Nanoparticles. *J. Solid State Chem.* **2009**, *182*, 2456–2460.
44. Jensen, K. M. Ø. Watching Materials Form: Particle Formation and Growth in Hydrothermal Synthesis. Ph.D. Thesis, Aarhus University, 2013.
45. Shannon, R. D. Revised Effective Ionic-Radii and Systematic Studies of Interatomic Distances in Halides and Chalcogenides. *Acta Crystallogr., Sect. A* **1976**, *32*, 751–767.
46. Silva, A. M. N.; Kong, X.; Parkin, M. C.; Cammack, R.; Hider, R. C. Iron(III) Citrate Speciation in Aqueous Solution. *Dalton Trans.* **2009**, *40*, 8616–8625.
47. Vukosav, P.; Mlakar, M.; Tomisic, V. Revision of Iron(III)-Citrate Speciation in Aqueous Solution. Voltammetric and Spectrophotometric Studies. *Anal. Chim. Acta* **2012**, *745*, 85–91.
48. Shweky, I.; Bino, A.; Goldberg, D. P.; Lippard, S. J. Syntheses, Structures, and Magnetic-Properties of 2 Dinuclear Iron(Iii) Citrate Complexes. *Inorg. Chem.* **1994**, *33*, 5161–5162.
49. Celic, T. B.; Jaglicic, Z.; Lazar, K.; Logar, N. Z. Structure and Magnetic Properties of a New Iron(II) Citrate Coordination Polymer. *Acta Crystallogr. Sect. B: Struct. Sci.* **2013**, *69*, 490–495.
50. Hussein, G. A. M. Physicochemical Investigation of the Decomposition Products of Ammonium Metal Carboxylates - Ammonium Ferric Citrate Hydrate. *Powder Technol.* **1994**, *80*, 265–270.

51. Gajbhiye, N. S.; Bhattacharya, U.; Darshane, V. S. Thermal-Decomposition of Zinc-Iron Citrate Precursor. *Thermochim. Acta* **1995**, *264*, 219–230.
52. Rayner-Canham, G.; Overton, T. *Descriptive Inorganic Chemistry*. W.H. Freeman and Company: New York, 2010.
53. Flynn, C. M. Hydrolysis of Inorganic Iron(III) Salts. *Chem. Rev.* **1984**, *84*, 31–41.
54. Magini, M.; Radnai, T. X-Ray-Diffraction Study of Ferric-Chloride Solutions and Hydrated Melt - Analysis of the Iron (III)-Chloride Complexes Formation. *J. Chem. Phys.* **1979**, *71*, 4255–4262.
55. Katsuki, H.; Komarneni, S. Microwave-Hydrothermal Synthesis of Monodispersed Nanophase α-Fe_2O_3. *J. Am. Ceram. Soc.* **2001**, *84*, 2313–2317.
56. Yu, J. G.; Yu, X. X.; Huang, B. B.; Zhang, X. Y.; Dai, Y. Hydrothermal Synthesis and Visible-Light Photocatalytic Activity of Novel Cage-like Ferric Oxide Hollow Spheres. *Cryst. Growth Des.* **2009**, *9*, 1474–1480.
57. Wang, S. B.; Min, Y. L.; Yu, S. H. Synthesis and Magnetic Properties of Uniform Hematite Nanocubes. *J. Phys. Chem. C* **2007**, *111*, 3551–3554.
58. Jing, Z. H.; Wu, S. H. Synthesis and Characterization of Monodisperse Hematite Nanoparticles Modified by Surfactants *via* Hydrothermal Approach. *Mater. Lett.* **2004**, *58*, 3637–3640.
59. Greaves, C. A Powder Neutron-Diffraction Investigation of Vacancy Ordering and Covalence in γ-Fe_2O_3. *J. Solid State Chem.* **1983**, *49*, 325–333.
60. Wang, J.; Sun, J. J.; Sun, Q.; Chen, Q. W. One-Step Hydrothermal Process to Prepare Highly Crystalline Fe_3O_4 Nanoparticles with Improved Magnetic Properties. *Mater. Res. Bull.* **2003**, *38*, 1113–1118.
61. Kodama, R. H. Magnetic Nanoparticles. *J. Magn. Magn. Mater.* **1999**, *200*, 359–372.
62. Kvick, A. Materials Science Research at the European Synchrotron Radiation Facility. *Nucl. Instrum. Methods Phys. Res. Sect. B* **2003**, *199*, 531–535.
63. Becker, J.; Bremholm, M.; Tyrsted, C.; Pauw, B.; Jensen, K. M. O.; Eltzholt, J.; Christensen, M.; Iversen, B. B. Experimental Setup for *in Situ* X-ray SAXS/WAXS/PDF Studies of the Formation and Growth of Nanoparticles in Near- and Supercritical Fluids. *J. Appl. Crystallogr.* **2010**, *43*, 729–736.
64. Hammersley, A. P.; Svensson, S. O.; Hanfland, M.; Fitch, A. N.; Hausermann, D. Two-Dimensional Detector Software: From Real Detector to Idealised Image or Two-Theta Scan. *High Pressure Res.* **1996**, *14*, 235–248.
65. Juhas, P.; Davis, T.; Farrow, C. L.; Billinge, S. J. L. PDFgetX3: A Rapid and Highly Automatable Program for Processing Powder Diffraction Data Into Total Scattering Pair Distribution Functions. *J. Appl. Crystallogr.* **2013**, *46*, 560–566.
66. Farrow, C. L.; Juhas, P.; Liu, J. W.; Bryndin, D.; Bozin, E. S.; Bloch, J.; Proffen, T.; Billinge, S. J. L. PDFfit2 and PDFgui: Computer Programs for Studying Nanostructure in Crystals. *J. Phys.: Condens. Matter* **2007**, *19*, 335219.